RSC Advances

ROYAL SOCIETY OF CHEMISTRY

PAPER

View Article Online
View Journal | View Issue

Check for updates

Cite this: *RSC Adv.*, 2026, **16**, 4090

Tunable structure–property engineering and visible-light photocatalytic performance of ZnO:TiO$_2$ nanocomposites synthesized *via* a solid-state route

Saliou Baïlo Diallo,[a] N. Khlifi, *[b] Modou Fall [a] and Hajer Guermazi [b]

Received 19th November 2025
Accepted 5th January 2026

DOI: 10.1039/d5ra08953k

rsc.li/rsc-advances

This study investigates the synthesis and characterization of $(1-x)$ZnO:(x)TiO$_2$ nanocomposites ($x = 0.01$ to 0.15) using the solid-state method. The structural properties are analyzed using X-ray diffraction (XRD). The XRD analysis reveals changes in phase composition, indicating TiO$_2$-dependent structural modifications. At low content ($x \leq 0.05$), Ti^{4+} ions dissolve substitutionally in the ZnO hexagonal structure. Beyond this threshold, the system reaches Ti saturation in ZnO and instead forms discrete Zn$_2$TiO$_4$ crystallites as a secondary phase. The crystallite size, estimated *via* the Debye–Scherrer model, decreases significantly from 50.8 nm to 44.5 nm with increasing TiO$_2$ content, and reaches 22.2 nm for 3% TiO$_2$ addition. Fourier transform infrared (FTIR) analysis likely confirms the Ti-doping of ZnO through the presence of Zn–O and Ti–O bonding. The band-gap energy was calculated using Tauc's model based on optical Reflectance data in the UV-Vis wavelength range. The direct band-gap transition exhibits a red-shift from 3.224 to 3.185 eV, while the indirect band-gap transition shows a more noticeable red-shift from 3.121 to 3.021 eV. The red-shift suggests band-gap narrowing, possibly due to defect states introduced by the Ti^{4+} cation. Furthermore, photocatalytic tests reveal that Ti-doping improves the methylene blue (MB) degradation efficiency under visible light. Notably, the ZnTi10% and ZnTi15% samples exhibit the highest degradation rates, reaching 87% with an apparent rate constant $K_{\text{app}} = 1.19 \times 10^{-2}$ min^{-1}, while pure ZnO and TiO$_2$ remain more active under visible light. This can be related to defects or interfacial states induced by Ti-doping, which act as electron–hole recombination centers.

1. Introduction

The rapid industrialization in recent decades has contributed to significant environmental challenges, particularly the contamination of water systems with hazardous dyes released mainly from the textile industries. These pollutants deteriorate water quality, disrupt aquatic ecosystems, and pose serious risks to human health.[1] Some dyes, especially azo dyes, are highly toxic and have been associated with severe environmental and health risks.[2,3] Untreated industrial effluents introduce harmful chemicals into aquatic environments and hinder sustainable development efforts.

To address dye pollution, various detection and remediation strategies have been developed. Analytical techniques such as spectrophotometry, high-performance liquid chromatography (HPLC), and mass spectrometry (MS) offer high accuracy but remain unsuitable for *in situ* monitoring due to their complexity and cost.[4] Conventional physicochemical treatment methods, including filtration, ion exchange, chemical precipitation, and adsorption, as well as electrochemical processes such as electrocoagulation, electro-flotation, and electrodecantation, are widely applied.[2,5] However, these approaches often suffer from limitations, including secondary pollution, high operational costs, and low removal efficiency. Consequently, advanced oxidation processes (AOP), particularly photocatalysis, have emerged as promising and sustainable alternatives for dye degradation.[6,7]

Among photocatalytic materials, metal oxide semiconductors, such as zinc oxide (ZnO) and titanium dioxide (TiO$_2$) have attracted considerable attention due to their multifunctional properties, photocatalytic activity, and applications in wastewater treatment and energy conversion.[7–13] ZnO is especially favored due to its low cost, environmental compatibility, and exceptional chemical and thermal stability.[14] It is widely utilized in diverse applications, including sunscreens, foods, paints, and batteries, owing to its multifunctionality and nature abundance.[15–17]

---

[a] Laboratory of Organic Physical Chemistry and Environmental Analyses, Department of Chemistry, Faculty of Sciences and Techniques, Cheikh Anta Diop University, Dakar, Senegal

[b] Laboratory of Materials for Energy and Environment, and Modeling (LMEEM), Faculty of Sciences, University of Sfax, B.P: 1171, 3038, Tunisia. E-mail: khlifinadia1991@gmail.com

ZnO is II–VI semiconductor with a direct band gap of 3.37 eV and an excitonic binding energy of 60 meV at room temperature.[18] ZnO nanoparticles exhibit enhanced photon absorption, a high surface area, and strong oxidative capability, making it highly effective in photocatalytic degradation of organic pollutants.[19,20] Moreover, its wide band gap, photostability, and high transparency in the visible range make it suitable for applications in optoelectronic, including light-emitting diodes,[21] photodetectors,[22] or photovoltaic cells.[23] Its high piezoelectric constant and chemical stability further support its use in spintronics and biosensors.[24,25] Structurally, ZnO crystallizes in three main phases: wurtzite (hexagonal), zinc blende (cubic), and rocksalt, with the wurtzite structure being the most thermodynamically stable at room temperature.[26]

TiO_2, similar to ZnO, is extensively studied as a photocatalyst due to its high photoactivity, chemical inertness, and strong oxidative potential. Both materials exhibit comparable band gap energies (3.27 eV for ZnO and 3.52 eV for TiO_2).[27] Importantly, the relative alignment of their valence and conduction band energy levels facilitates efficient charge carrier separation when combined in a heterojunction system.[28] As a result, ZnO–TiO_2 nanocomposites have demonstrated enhanced photocatalytic performance through reduced electron–hole recombination and extended light absorption ranges.[27–30]

Various synthesis techniques have been employed to fabricate $(1-x)$ZnO:$(x)$$TiO_2$ nanocomposites, including sol–gel processing,[31] co-preparation,[32] and solid-state reactions.[31–33] Among these methods, the solid-state approach is particularly attractive due to its simplicity, low cost, and use of readily available starting materials.[33]

In the present study, $(1-x)$ZnO:$(x)$$TiO_2$ nanoparticles were synthesized through the solid-state method with varying of TiO_2 molar concentrations. The influence of TiO_2 incorporation on the structural, optical, and photocatalytic properties of the prepared samples. The photocatalytic performance is evaluated through methylene blue (MB) degradation under visible light irradiation, and the observed activity is correlated with the structural and optical modifications induced by TiO_2 addition.

2. Experimental

2.1. Samples synthesis

$(1-x)$ZnO:$(x)$$TiO_2$ nanocomposites were prepared by means of a conventional solid-state process, using pure ZnO and TiO_2 powders as starting materials. The raw oxides were purchased from Sigma Aldrich. For each composition, the appropriate mass of TiO_2 and ZnO powders were weighed and thoroughly mixed. The mixture was ground for one hour to achieve homogeneity of the powders. The resulting powders were calcined in a furnace at 400 °C for four hours. After calcination, the powders was reground for 1 h 30 min to achieve thin particles with better uniformity. Finally, the samples were sintered at 900 °C, followed by additional grinding step for 30 minutes for each sample. The samples were labeled according to Table 1 for easy following up.

Table 1 Samples labels and the corresponding composition

Sample code	Composition
ZnO	ZnO
TiO_2	TiO_2
ZnTi1%	(0.99)ZnO:(0.01)TiO_2
ZnTi2%	(0.98)ZnO:(0.02)TiO_2
ZnTi3%	(0.97)ZnO:(0.03)TiO_2
ZnTi5%	(0.95)ZnO:(0.05)TiO_2
ZnTi10%	(0.90)ZnO:(0.1)TiO_2
ZnTi15%	(0.85)ZnO:(0.15)TiO_2

2.2. Material characterization techniques

The crystalline structure of the $(1-x)$ZnO:$(x)$$TiO_2$ powders was characterized using an X-ray diffractometer (XRD) (Bruker's D8 Advance diffractometer) equipped with CuKα1 radiation (λ = 1.5406 Å), operating at 40 kV and 40 mA. The molecular vibration energies of the samples is provided *via* Fourier Transform Infrared (FTIR) experiments, investigated with a BRUKER spectrophotometer in the 400–4000 cm^{-1} range. The morphologies of the composites were observed using Scanning Electron Microscopy (SEM, model JEOL JSM7100F) coupled with Energy Dispersive Spectroscopy (EDX), using double-faced adhesive carbon pads (AGG3347N from Agar Scientific). In order to estimate the average grain size, the Image J software was then used. The optical band gap energies of $(1-x)$ZnO:$(x)$$TiO_2$ nanocomposites were determined through the UV-visible Diffuse Reflectance Spectrophotometer (DRS, model Perkin-ELMER 365, 300–800 nm), then the Kubelka–Munk formula was used for the estimation of band gap energy.

2.3. Photocatalytic activity evaluation

The photocatalytic activity of $(1-x)$ZnO:$(x)$$TiO_2$ powders was evaluated by monitoring the degradation of methylene blue (MB) aqueous solution under visible light irradiation. MB dye was selected as a model pollutant due to its non-biodegradable nature and its resistance to conventional treatment methods.[34] 50 mL of MB solution at a concentration of 10 mg L^{-1} was mixed with 50 mg of the photocatalyst. The suspension was magnetically stirred in the dark environment at room temperature for 60 minutes to establish adsorption–desorption equilibrium between the dye molecules and the catalyst surface. Subsequently, the suspension was exposed to visible light irradiation under continuous stirring. A sample was collected immediately before illumination to serve as the initial reference ($t = 0$ min). At regular intervals of 15 minutes, 3 mL aliquots were withdrawn, filtered, and centrifuged to remove the catalyst particles. The degradation of MB was monitored by measuring its characteristic absorption peak intensity (around 664 nm) using a UV-visible spectrophotometer (SP-UV-300).

The degradation efficiency (D) was calculated using eqn (1):

$$D(\%) = \left(\frac{C_0 - C_t}{C_0}\right) \times 100 = \left(\frac{A_0 - A_t}{A_0}\right) \times 100 \tag{1}$$

where C_0 and A_0 are the initial concentration and initial absorbance of methylene blue, respectively, and C_t and A_t are the concentration and absorbance at irradiation time t.

3. Results and discussions

3.1. Structural and compositional analyses

The phase composition and crystallinity of synthesized $(1-x)$ZnO:(x)TiO$_2$ powders ($x = 0.0$–0.15, 1) were characterized by X-ray diffraction analysis.

3.1.1. Revised XRD analysis. Fig. 1 presents the X-ray diffraction patterns of $(1-x)$ZnO:(x)TiO$_2$ composites across the complete composition range ($x = 0$–1).

Fig. 1 presents the X-ray diffraction patterns of $(1-x)$ZnO:(x)TiO$_2$ composites ($x = 0$–1). For pure ZnO ($x = 0$), all diffraction peaks correspond to the hexagonal wurtzite structure (JCPDS 01-080-0075), with characteristic reflections at 31.97° (100), 34.65° (002), 36.42° (101), 47.78° (102), and 56.83° (110), consistent with literature.[35,36] Pure TiO$_2$ ($x = 1$) exhibits a mixed-phase composition, showing anatase reflections (JCPDS 00-021-1272, *I*4$_1$/*amd* space group) at 25.60° (101), 38.17° (004), and 48.40° (200), along with a rutile phase peak (JCPDS 01-082-0514) at 27.62° (110).[37] For intermediate compositions (0.01–0.15), systematic evolution of the diffraction patterns is observed, manifested through progressive shifts in peak positions, variations in relative intensities, and changes in phase composition, indicating TiO$_2$-dependent structural modifications.

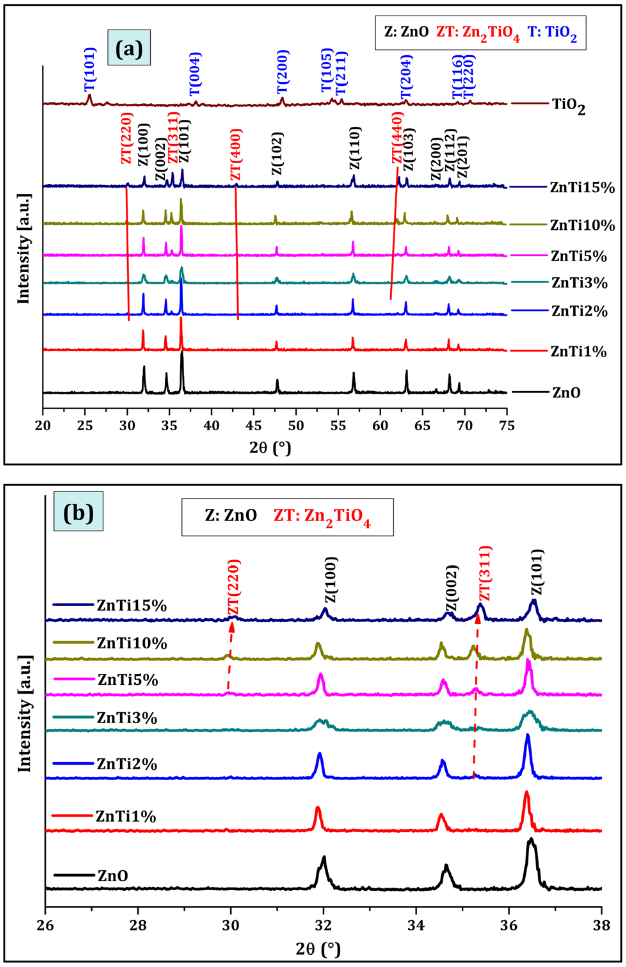

Fig. 1 (a) XRD patterns of $(1-x)$ZnO:(x)TiO$_2$ nanocomposites, showing shift in ZnO peaks due to Ti^{4+} incorporation. (b) Enlarged diffractograms of the prominent peaks, highlighting the appearance of Zn$_2$TiO$_4$ as a secondary phase at higher Ti content.

X-ray diffraction analysis reveals a structural transformation in $(1-x)$ZnO:(x)TiO$_2$ composites as TiO$_2$ content increases from $x = 0.01$ to 0.15 (Fig. 1). For low compositions ($x \leq 0.05$), the diffraction patterns predominantly retain the wurtzite ZnO structure, though distinct peak shifts are observed (Fig. 1b). These angular displacements, particularly evident in the (101) reflection, demonstrate lattice strain resulting from successful Ti^{4+} incorporation into the ZnO matrix. The observed distortion arises from the significant ionic radius mismatch between the incorporated Ti^{4+} (0.605 Å) and the host Zn^{2+} (0.74 Å) cations.[38]

At higher TiO$_2$ concentrations ($x \geq 0.10$), four new diffraction peaks emerge at 29.95° (220), 35.24° (311), 42.92° (400), and 62.11° (440), unambiguously identifying the formation of cubic Zn$_2$TiO$_4$ spinel phase ($Fd\bar{3}m$ space group, JCPDS 00-025-1164).[38,39] This phase transformation occurs through cationic redistribution, where Zn^{2+} ions migrate into octahedral sites within TiO$_2$-rich regions while steric constraints prevent Ti^{4+} incorporation into ZnO tetrahedral sites.[38,40,41] Thus, the solid-state reaction between excess ZnO and TiO$_2$ drives spinel formation, yielding a biphasic system containing both strained ZnO and crystalline Zn$_2$TiO$_4$ phases. This solid-state reaction occurring during high-temperature sintering can be expressed as:[42]

$$2\mathrm{ZnO} + \mathrm{TiO_2} \rightarrow \mathrm{Zn_2TiO_4} \tag{2}$$

This composition-dependent structural evolution matches previous observations in Ti-doped ZnO systems.[38,40] The results suggest a clear evolution of phases with increasing TiO$_2$ content. At low doping levels ($x < 0.05$), Ti^{4+} ions are effectively incorporated into the ZnO lattice, causing strain but no significant formation of secondary phases. At higher doping levels ($x \geq 0.05$), the system evolves to a multiphase structure, generating ZnO/Zn$_2$TiO$_4$ composites.[40,42] This indicates a saturation point beyond which Ti^{4+} ions no longer integrate into the ZnO lattice but instead contribute to the formation of separate phases.[43,44]

To determine structural parameters, the lattice constants (a, c) and unit cell volume (V) of hexagonal ZnO were calculated from the (100) and (002) XRD peak positions using the following equations:

$$\frac{1}{d_{(hkl)}{}^2} = \frac{4}{3}\left(\frac{h^2 + k^2 + hk}{a^2}\right) + \frac{l^2}{c^2} \tag{3}$$

$$a = b = \frac{\lambda}{\sqrt{3}\sin\theta_{(100)}} \tag{4}$$

$$c = \frac{\lambda}{\sin\theta_{(002)}} \tag{5}$$

$$V = 0.866 \times a^2 \times c \tag{6}$$

where θ is the Bragg's angle, and λ is the X-ray wavelength of the Cu-Kα line ($\lambda = 1.5406$ Å).

The Zn–O bond length (L) was calculated using this equation:[45]

$$L = \sqrt{\left[\frac{a^3}{3} + (0.5-u)^2 \times c^2\right]} \tag{7}$$

where $u = \dfrac{a^2}{3c^2} + 0.25$.

The micro-strain (ε) and the stress σ (GPa) in the crystallite's plane were estimated *via* these expressions:[45,46]

$$\varepsilon = \frac{\beta}{4\tan\theta_{(101)}} \tag{8}$$

$$\sigma = 233\left(\frac{c_{\text{bulk}} - c}{c_{\text{bulk}}}\right) \tag{9}$$

where c and c_{bulk} are the measured and the strain-free lattice parameters of ZnO phase ($c_{\text{bulk}} = 5.2061$ Å), respectively. β is the full width at half maximum (FWHM) of the diffraction peaks.

The lattice parameters and the volume of unit cell of the anatase phase of TiO_2 were calculated using the basic equations for tetragonal crystal structure:[47]

$$\frac{1}{{d_{(hkl)}}^2} = \frac{h^2 + k^2}{a^2} + \frac{l^2}{c^2} \tag{10}$$

$$V = a^2 \times c \tag{11}$$

The crystallite size (D) was calculated using the most intense (101) diffraction peak by means of the Debye–Scherrer formula:[48,49]

$$D = \frac{0.94\lambda}{\beta\cos\theta} \tag{12}$$

Table 2 shows slight variations of lattice parameters due to the incorporation of Ti ions into the ZnO lattice, which induces lattice distortion due to ionic radius mismatch between Zn^{2+} (0.74 Å) and Ti^{4+} (0.605 Å).[50] At lower doping levels (1–10%), the lattice expands slightly to accommodate Ti ions, while at higher doping levels (15%), the sharp decrease in lattice parameters indicates possible lattice relaxation, phase segregation, or the formation of secondary phases.[51]

The variation of crystallite size and micro-strain as a function of TiO_2 doping in ZnO reveals significant structural changes. Notably, the crystallite size (Table 2) shows a decrease at ZnTi3% reaching about 22 nm, simultaneously with the highest micro-strain (ε) value, giving rise to a constrained ZnO structure. At higher doping levels, such as ZnTi15%, the observed changes may be attributed to the formation of secondary phases or partial relaxation of the lattice.[38] These structural variations are critical in determining the material's photocatalytic and electronic properties, with ZnTi3% and ZnTi15% representing points of interest for further optimization.[51] Moreover, the c/a ratio maintains the value of 1.6 (Table 2), which is the standard value for hexagonal cell $c/a = 1.60$.[49] Thereafter, the Ti content does not alter the hexagonal structure of ZnO NPs. Besides, the slight change in the Zn–O bond length can be related to the change in lattice parameters. Therefore, the obtained results prove the successful incorporation of Ti element into ZnO host matrix, which will be confirmed by EDX analysis.

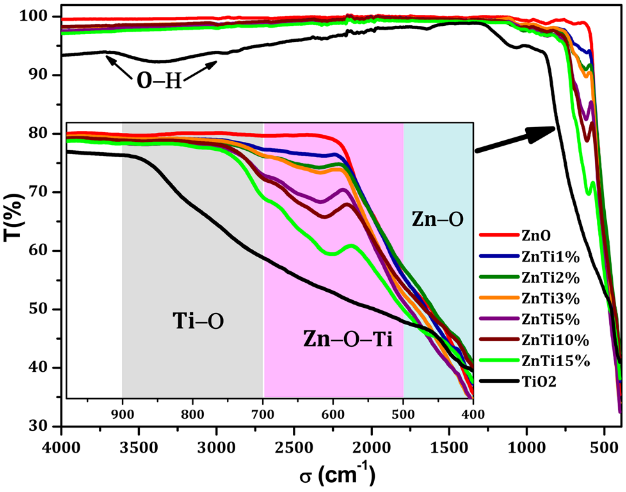

Fig. 2 FTIR Spectra of $(1-x)ZnO:(x)TiO_2$ composites highlight the metal–oxygen vibrational modes.

3.2. FTIR analysis

FTIR is a non-destructive technique used to analyze the chemical bonding in materials. In Fig. 2, the FTIR spectra of the $(1-x)ZnO:(x)TiO_2$ composites provide valuable insights into the vibrational modes and structural features of the synthesized materials.

The absorption bands observed in the range of 400–500 cm^{-1} are attributed to characteristic Zn–O stretching vibrations, consistent with literature reports of Zn–O modes around 430–

Table 2 Structural parameters of ZnO as a function of TiO_2 content

Samples	$a = b$ (Å)	c (Å)	V (Å^3)	c/a	u	L (Å)	σ (GPa)	D (nm)	ε
ZnO	3.157	5.057	43.658	1.601	0.3799	3.295	6.682	50.83	0.22
ZnTi1%	3.166	5.073	44.031	1.602	0.3798	3.309	5.970	44.47	0.25
ZnTi2%	3.162	5.067	43.865	1.602	0.3797	3.302	6.206	59.29	0.20
ZnTi3%	3.159	5.065	43.781	1.603	0.3797	3.300	6.307	22.24	0.51
ZnTi5%	3.162	5.069	43.877	1.603	0.3797	3.302	6.142	59.30	0.19
ZnTi10%	3.166	5.073	44.036	1.602	0.3798	3.309	5.932	48.66	0.22
ZnTi15%	3.151	5.049	43.414	1.602	0.3798	3.286	7.029	44.50	0.25
TiO_2	3.758	9.455	133.55	—	—	—	—	21.66	0.74

500 cm^{-1} in ZnO and ZnO/TiO$_2$ systems.[52–55] Specifically, bands near ∼500 cm^{-1} are widely assigned to Zn–O vibrations in binary oxide systems.[56] At lower doping levels ($x = 0.01$ to 0.05), these bands dominate, aligning with the XRD results that indicate ZnO as the primary phase, with minor lattice distortions caused by the substitution of Ti^{4+} ions into the ZnO lattice.[56]

As the Ti doping concentration increases ($x \geq 0.10$), new features appear in the 500–700 cm^{-1} region, which can be assigned to Zn–O–Ti vibration modes associated with the formation of the Zn$_2$TiO$_4$ spinel phase. Similar bands in this region (typically 550–680 cm^{-1}) have been reported for Zn$_2$TiO$_4$ and ZnO–TiO$_2$ composite systems.[54,57] The increasing intensity of these bands with Ti content confirms the gradual evolution from ZnO-dominated structure to a mixted-phase system composed of ZnO and Zn$_2$TiO$_4$.[58]

In the 700–900 cm^{-1} range, a broad vibrational band is attributed to Ti–O stretching modes, which have been reported in TiO$_2$ and ZnO–TiO$_2$ systems around ∼700−850 cm^{-1}.[56] The broad absorption bands in the 900–1500 cm^{-1} region are associated with surface hydroxyl groups adsorbed on the surface of nanoparticles, while the broad bands in the 1500–3500 cm^{-1} region are attributed to O–H stretching vibrations, indicating surface hydration or adsorbed water molecules.[59,60] The presence of surface hydroxyl groups is particularly significant, as they play a crucial role in photocatalytic activity by facilitating the generation of reactive oxygen species (ROS) under light irradiation.[61,62]

3.3. FESEM/EDX analysis

The surface morphology of the prepared samples was investigated by Field Emission Scanning Electron Microscopy (FESEM) and the images acquired are shown in Fig. 3a.

The FESEM image of pure ZnO revealed a heterogeneous distribution of rod-like nanostructures, whereas pure TiO$_2$ exhibited quasi-spherical nanoparticles (Fig. 3a). Incorporation of TiO$_2$ into the ZnO matrix significantly influenced the morphology of the resulting nanostructures, particularly their size and shape, leading to the formation of nanosheet structures. The observed increase in particle size at low doping concentrations implies that Ti ions may promote anisotropic growth along specific crystallographic axes, favoring the formation of 2D-elongated structures.[63] Enhanced optoelectronic properties of Ti-doped ZnO nanorods have also been reported for photodetector applications.[64] Overall, these observations indicate that the Ti content modulates the growth dynamics of ZnO nanostructures.[65]

In addition to changes in average length, the standard deviation (SD) values provide insight into the size distribution and structural uniformity of the nanorods (Fig. 3b and Table 3). The SD for pure ZnO was 41.07 nm, reflecting a relatively broad distribution of lengths. With Ti doping, a slight reduction in SD was observed, especially at higher doping levels (36.88 nm for ZnTi15%). This trend suggests that higher Ti content may contribute to more uniform particle growth, potentially due to better control over nucleation kinetics or reduced aggregation

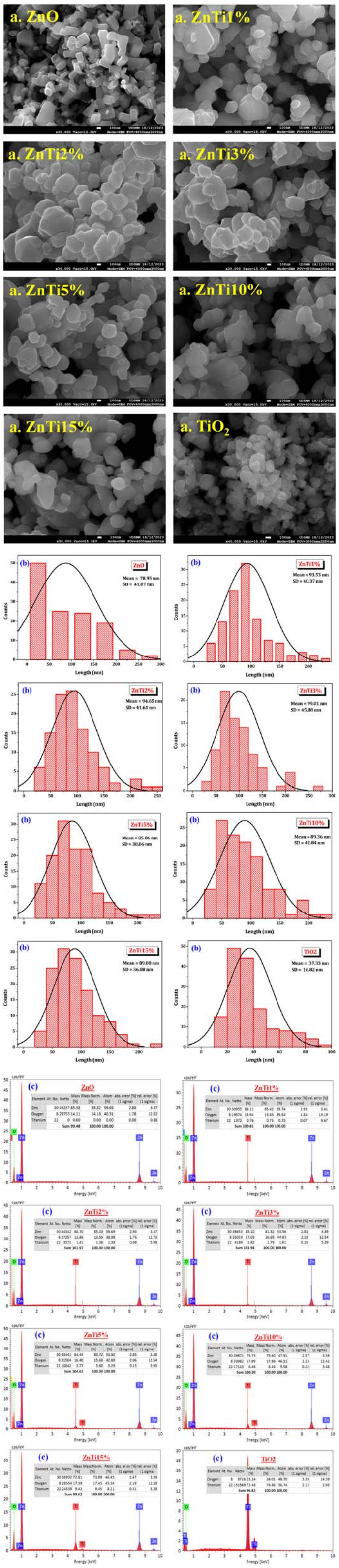

Fig. 3 (a) FESEM pictures of (1 − x)ZnO:(x)TiO$_2$ nanostructures, (b) size distribution histogram showing the length distributions fitted to Gaussian curves and (c) EDX analysis of samples; the atomic and weight percentage of Zn, Ti and O are depicted in the inset.

Table 3 Average particle size and standard deviations (SD) of $(1-x)$ ZnO:(x)TiO$_2$ nanostructured samples, determined using the Image J software

Samples	Average particle size (nm)	SD (nm)
ZnO	78.95	41.07
ZnTi1%	93.53	40.37
ZnTi2%	94.65	41.61
ZnTi3%	99.01	45.08
ZnTi5%	85.06	38.06
ZnTi10%	89.36	42.84
ZnTi15%	89.08	36.88
TiO_2	37.33	16.82

effects.[66] Interestingly, pure TiO_2 particles exhibited the smallest average length (37.33 nm) and the lowest SD (16.82 nm), which is consistent with their typical spherical or near-spherical morphology rather than rod-like structures.[67]

Overall, Ti-doping in ZnO modifies both the average length and distribution of the resulting nanostructures. Low levels of Ti enhance axial growth, while higher doping concentrations contribute to size homogenization. These morphological variations may influence the surface area and interfacial characteristics of the materials, which, in combination with phase composition and charge carrier dynamics, can affect their photocatalytic or anti-adhesive performance in subsequent applications.[68,69]

Energy dispersive X-ray (EDX) analysis was performed to investigate the elemental composition of $(1-x)$ZnO:(x)TiO$_2$ nanocomposites for different TiO_2 contents (Fig. 3c). The EDX spectra confirm the presence of Zn, Ti and O elements in all analyzed samples, with no detectable impurity-related peaks, indicating the chemical purity of the synthesized materials. For low TiO_2 contents, Ti signals appear with relatively low intensity, consistent with Ti^{4+} incorporation into the ZnO lattice. As the TiO_2 concentration increases, the Ti peak intensity increases systematically, accompanied by a corresponding decrease in Zn intensity, reflecting the progressive enrichment of Ti in the composite. At higher TiO_2 contents, the measured Zn/Ti atomic ratios deviate from those expected for a single-phase solid solution, which is consistent with the formation of Zn_2TiO_4 as a secondary phase, as evidenced by XRD analysis. These results confirm the composition-dependent evolution of the ZnO–TiO_2 system and support the coexistence of Ti-saturated ZnO and Zn_2TiO_4 phases at higher TiO_2 concentrations.

3.4. Optical properties

3.4.1. UV-vis absorption analysis. The diffuse reflectance spectra of the prepared $(1-x)$ZnO:(x)TiO$_2$ provided valuable insights into their optical properties, complementing the structural changes observed in the XRD analysis (Fig. 4).

The ZnO sample exhibits a sharp increase in reflectance near 380 nm, corresponding to its characteristic band-gap energy.[60] Similarly, pure TiO_2 shows a sharp reflectance edge at approximately 360 nm, consistent with its intrinsic optical behavior.[60]

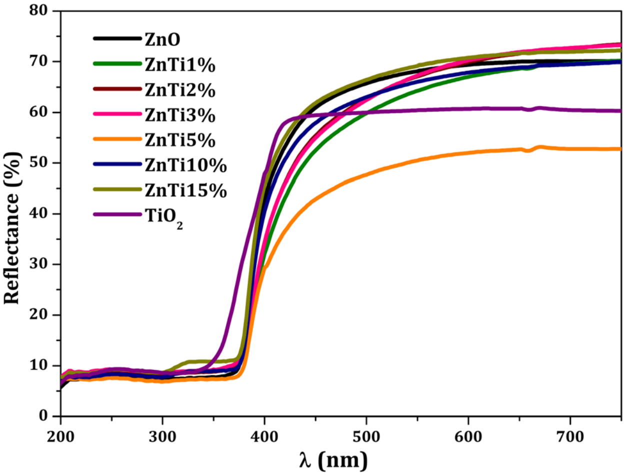

Fig. 4 Diffuse reflectance spectra of $(1-x)$ZnO:(x)TiO$_2$ samples.

At lower TiO_2 concentrations ($x < 0.05$), the reflectance spectra remain largely similar to that of pure ZnO, with only minor variations (Fig. 4). This aligns with the XRD results, where ZnO remains the dominant phase, and the observed 2θ shifts suggest lattice distortion due to the incorporation of Ti^{4+} ions into the ZnO lattice.[38]

Notably, the ZnTi5% sample exhibits a distinct reflectance profile compared to other samples, with a higher reflectance across the UV-Vis region. This behavior may be related to enhanced interaction between ZnO and TiO_2 phases or the formation of localized defect states.[70,71] Overall, the optical and structural analyses demonstrate the evolution of the material properties with increasing TiO_2 content.

3.4.2. Determination of the optical band-gap. The optical band-gap energy (E_g) of the $(1-x)$ZnO:(x)TiO$_2$ nanocomposites was determined using the Tauc formalism:

$$(F(R) \times h\nu)^n = A(h\nu - E_g) \tag{13}$$

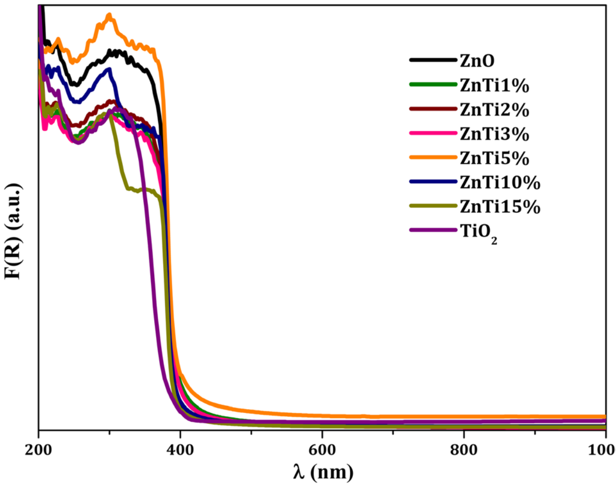

Fig. 5 Kubelka–Munk function spectra of $(1-x)$ZnO:(x)TiO$_2$ samples as a function of wavelength (λ) in nm.

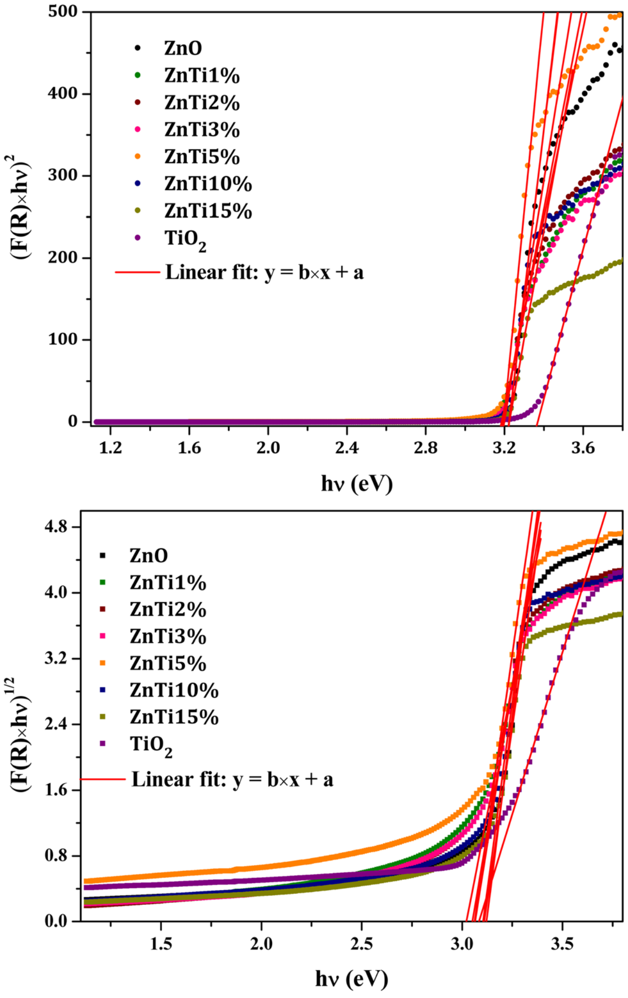

Fig. 6 Graphical representation of $(F(R) \times h\nu)^n$ as a function of $h\nu$ for the various $(1-x)$ZnO:(x)TiO$_2$ samples for $n = 2$ and $n = 1/2$ respectively.

where $h\nu$ is the photon energy, and. $n = 2$ or $n = 1/2$ correspond to direct and indirect allowed transitions, respectively.[4,72] R is the diffuse reflectance, $F(R)$ is the Kubelka–Munk (K–M) function:

$$F(R) = \frac{(1-R)^2}{2R} \tag{14}$$

As shown in Fig. 5, all samples exhibit intense absorption peaks in the UV region, accompanied by a shift of the absorption edge toward higher wavelengths, indicating a red shift. This behavior is consistent with previous reports[73] and can be attributed to band-gap narrowing.[74] The presence of two distinct absorption edges suggests contributions from two crystalline phases, in agreement with the coexistence of ZnO and Zn_2TiO_4 phases observed by XRD.[75]

The band-gap values were obtained by extrapolating the linear region of the $(F(R) \times h\nu)^n$ *versus* $h\nu$ plots to the photon energy axis at $(F(R) \times h\nu)^n = 0$ (Fig. 6).[76,77]

The experimental band-gap values extracted from Fig. 6 are summarized in Table 4.

Table 4 Band-gap energy values for direct and indirect transitions of the various samples

Samples	$(F(R) \times h\nu)^2$	Adj. R-square	$(F(R) \times h\nu)^{1/2}$	Adj. R-square
ZnO	3.224	0.96	3.121	0.99
ZnTi1%	3.185	0.98	3.021	0.98
ZnTi2%	3.199	0.98	3.064	0.99
ZnTi3%	3.191	0.97	3.050	0.99
ZnTi5%	3.196	0.97	3.061	0.99
ZnTi10%	3.222	0.99	3.104	0.99
ZnTi15%	3.224	0.99	3.110	0.99
TiO_2	3.368	0.99	3.083	0.99

The band-gap energy values presented in Table 4 provide insight into the electronic transitions within the pure and doped ZnO–TiO_2 samples. These values reveal how doping affects the structural and optical properties of the materials.

For pure ZnO, the band-gap energy is 3.224 eV for direct transitions and 3.121 eV for indirect transitions. These values are consistent with the intrinsic semiconducting properties of ZnO.[78] On the other hand, pure TiO_2 exhibits a higher band-gap energy of 3.368 eV for direct transitions and 3.083 eV for indirect transitions, which aligns with the known wide band-gap of anatase TiO_2.[79,80] These differences reflect the distinct electronic structures of ZnO and TiO_2.

At low doping levels ($x \leq 0.05$), the band-gap energies of the ZnO-based samples show minor variations. For example, ZnTi1% has a direct band-gap of 3.185 eV and an indirect band-gap of 3.021 eV, while ZnTi5% has a direct band-gap of 3.196 eV and an indirect band-gap of 3.061 eV. These slight shifts can be attributed to lattice distortions caused by the incorporation of Ti^{4+} ions into the ZnO lattice.[81] Despite these changes, the adjusted R-square values remain close to 1.00 (ranging from 0.97 to 0.99), indicating a high degree of accuracy in the fitting process.

At intermediate doping levels ($x \geq 0.10$), more pronounced changes in the band-gap energies are observed. For instance, ZnTi10% exhibits a direct band-gap of 3.222 eV and an indirect band-gap of 3.104 eV, while ZnTi15% shows a direct band-gap of 3.224 eV and an indirect band-gap of 3.110 eV. This trend suggests the emergence of the Zn_2TiO_4 phase, which significantly influences the electronic structure of the material.[38] The consistently high-adjusted R-square values ($\geq$0.99) across all samples further validate the reliability of the measurements. Overall, the band-gap energies for direct transitions are consistently higher than those for indirect transitions across all samples, a typical characteristic of semiconductors.[82] The progressive doping of Ti into ZnO results in slight reductions in the band-gap energies, reflecting the structural and electronic modifications induced by the doping.[75] These findings highlight the tunability of the optical properties of ZnO–TiO_2 composites, making them promising for applications in photocatalysis and optoelectronics.[14]

It's important to note that ZnTi1% has the lowest energy value compared with the other samples, with a direct band-gap of 3.185 eV and an indirect band-gap of 3.021 eV. This red shift could be explained by the narrowing of the band-gap energy

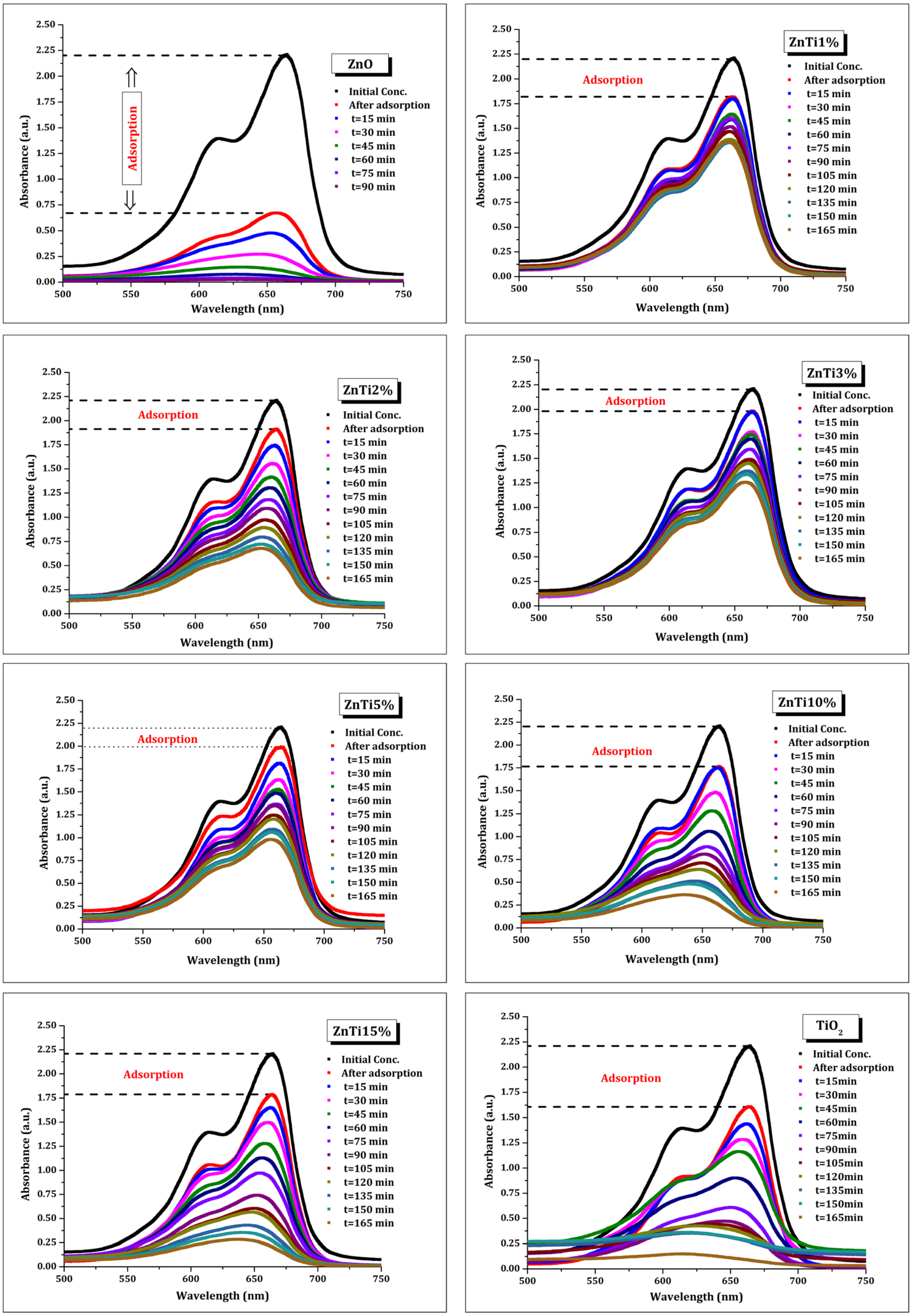

Fig. 7 Evolution of UV-Vis absorption spectra of MB as a function of time in the presence of (1 − x)ZnO:(x)TiO_2 samples under visible light irradiation.

resulting from the incorporation of Ti into the ZnO matrix.[76] In fact, this decrease in band-gap energy is probably due to the increase in crystal defects, notably oxygen vacancies, which can act as electron acceptors below the ZnO conduction band, thereby affecting its structure. These defects, which are naturally present in ZnO, lead to the generation of localized energy

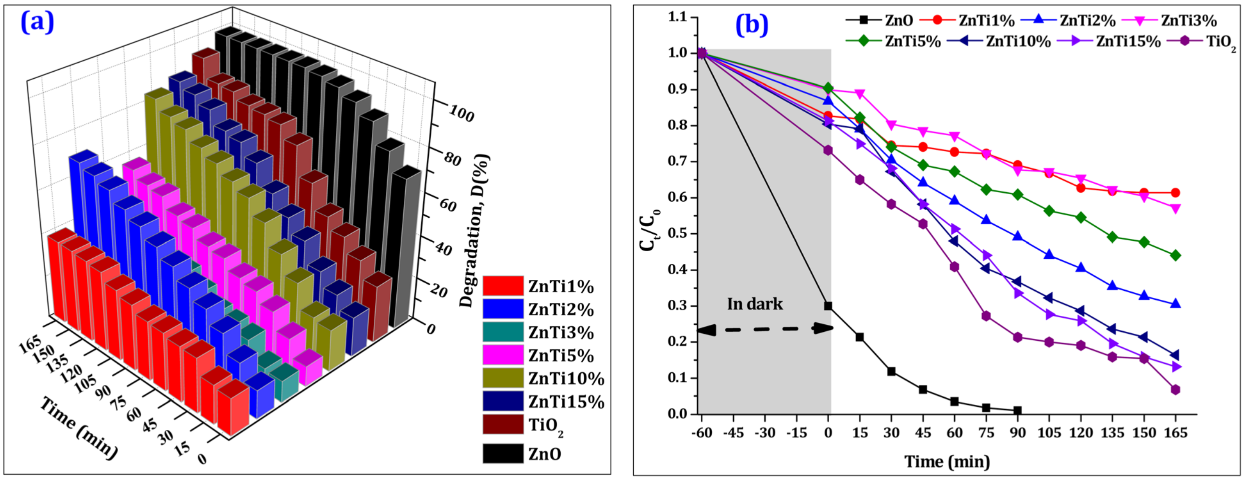

Fig. 8 (a) Comparison of the degradation efficiencies (D (%)) as a function of reaction time, (b) the concentration ratio C_t/C_0 of MB as a function of irradiation time for all the catalysts.

levels within the band-gap, resulting in a red shift.[83] Furthermore, the red shift can be explained by hybridization between the transition metal atoms and the Zn atom.[84] In fact, in the work of Selvinsimpson *et al.*, tin-doped ZnO samples show a decrease in electron density leading to a reduction in the band-gap due to electron exchanges of the 3d–4s and 4d–5s orbitals of Sn-doped ZnO.[85] These latter interpretations are in agreement with those made in the work of Zhao *et al.*, where the redshift of the absorption edge of Ni-doped ZnO samples was explained by the strong interaction of sp–d electron exchange.[86]

3.5. Photocatalytic study

3.5.1. Degradation of methylene blue. The photocatalytic performance of $(1-x)$ZnO:(x)TiO$_2$ nanopowders were evaluated by the de-colorization of MB aqueous solutions under visible light irradiation. Optical absorption spectra were recorded in different time intervals (15 min) up to 165 min at room temperature. The obtained results are presented in Fig. 7.

The results obtained (Fig. 7) highlighted the absorbance decrease with the duration of visible light exposure.

The photocatalytic degradation efficiency (D%) of methylene blue (MB) over time for ZnO photocatalysts modified with various TiO$_2$ weight percentages (1%, 2%, 3%, 5%, 10%, and 15%) is presented in Fig. 8a. Fig. 8b shows the corresponding C_t/C_0 ratios as a function of irradiation time, derived from absorbance measurements.

The degradation profiles reveal a clearl enhancement in photocatalytic performance upon incorporation of TiO$_2$ into the ZnO matrix, with an optimal loading observed at higher Ti concentrations. Notably, the ZnTi10% and ZnTi15% samples exhibit the highest degradation efficiencies, approaching complete MB removal after extended illumination. In contrast, the ZnTi3% sample displays the lowest efficiency, suggesting that at this loading, TiO$_2$ may induce less favorable effects, such as incomplete heterojunction formation, partial surface coverage, or increased charge carrier recombination.[69,87]

These trends correlate closely with particle size evolution (Fig. 9).

Pure ZnO and TiO$_2$ show relatively high MB degradation (~99% and 92%, respectively), whereas low Ti-doped samples (1–3%) exhibit significantly lower efficiencies (~38–70%). This reduction is likely due to insufficient heterojunction formation, limited surface-active sites, and enhanced recombination of photogenerated electron–hole (h^+–e^-) pairs. Higher Ti loadings (10–15%) result in optimal particle size and morphology, favoring effective heterojunction formation, improved charge separation, and enhanced surface activityn leading to higher MB degradation (84–87%).

Overall, the photocatalytic performance demonstrates a non-linear relationship with particle size and Ti content, emphasizing the importance of controlled morphology and heterojunction engineering in maximizing photocatalytic efficiency.

3.5.2. Kinetics modeling. In the present study, ZnO was combined with varying percentages of TiO$_2$ to evaluate the

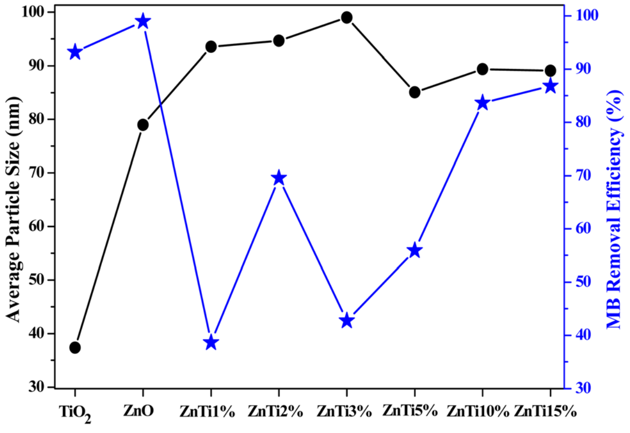

Fig. 9 Variation of average particle size (from FESEM analysis) and methylene blue removal efficiency as a function of TiO$_2$ content for $(1-x)$ZnO:(x)TiO$_2$ nanostructured samples.

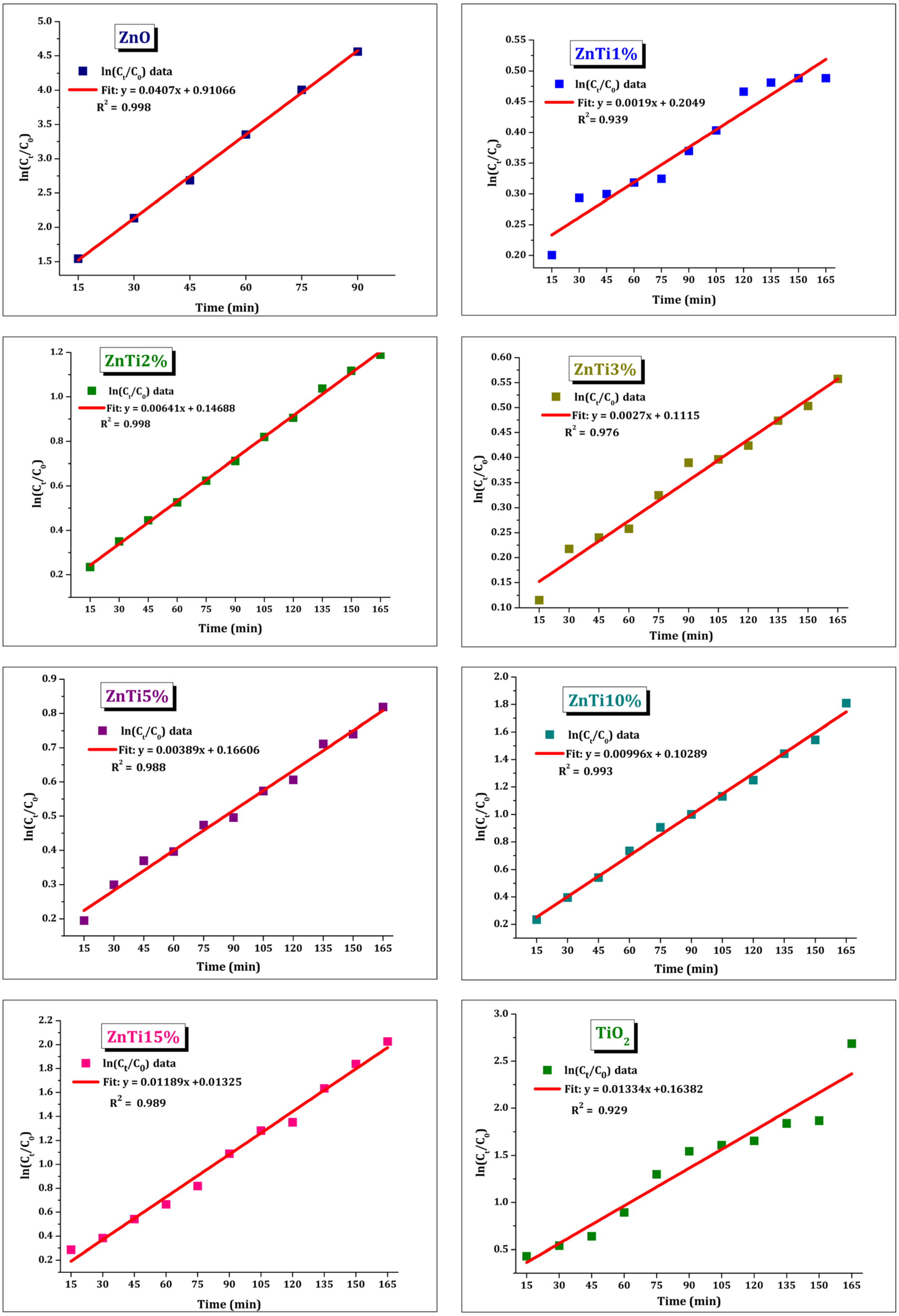

Fig. 10 Modeling of MB dye photodegradation kinetics by means of (L–H) model.

photocatalytic performance of the resulting composites. Investigating the kinetics of photocatalytic degradation is crucial to gaining insights into the reaction mechanisms and efficiency under specific experimental conditions.[88] Compared to suspended systems, kinetic analysis in systems involving immobilized or composite photocatalysts such as ZnO/TiO_2 mixtures can be more complex due to reduced light penetration within the catalyst matrix and potential internal mass transport

Table 5 The parameters values of pseudo-first order (PFO) model fitted

Model	PFO		
Samples	Velocity constant, K_{app} ($\times 10^{-3}$ min^{-1})	Half life time, $t_{1/2}$ (min)	R^2
ZnO	40.7	17	0.998
ZnTi1%	1.9	364	0.940
ZnTi2%	6.4	107	0.998
ZnTi3%	2.7	256	0.976
ZnTi5%	3.8	178	0.988
ZnTi10%	9.9	70	0.993
ZnTi15%	11.89	58	0.989
TiO_2	13.34	52	0.929

limitations.[89] To interpret the reaction behavior, the Langmuir–Hinshelwood (L–H) kinetics was the most widely used model for explaining the kinetics of heterogeneous photocatalytic processes.

The Langmuir–Hinshelwood (L–H) model is usually used to describe the kinetics of photocatalytic reactions of organics.[90,91] It relates the degradation rate (r) to reactant concentration in water at time t (C), which is expressed according to eqn (15):[92]

$$r = -\frac{dC}{dt} = \frac{K_r K_{ad}}{1 + K_{ad} C} \tag{15}$$

where K_r is the rate constant and K_{ad} is the adsorption equilibrium constant.

When the absorption is relatively weak and/or the reaction concentration is low, eqn (15) can be simplified to the pseudo-first order (PFO) kinetics with an apparent first-order rate constant K_{app}:

$$\ln(C_t) = -K_{app}t + \ln(C_0) \tag{16}$$

where C_0 is the initial concentration, C_t is the concentration at time t, and K_{app} represents the apparent rate constant (min^{-1}). Plotting $\ln(C_0/C)$ *versus* illumination time (t) yields a straight line, and the slope is the apparent rate constant K_{app}.

3.5.2.1 *Half-life time reaction.* The calculation of half-life time reaction ($t_{1/2}$) is one of the most useful means to evaluate the reaction rate of first order kinetic. At the half-life of reaction, $C = 0.5C_0$. For the reaction with the pseudo-first order, the half-life ($t_{1/2}$) time can be calculated as the following:

$$t_{1/2} = \frac{\ln(2)}{K_{app}} \approx \frac{0.693}{K_{app}} \tag{17}$$

This is independent of the initial concentration.

3.5.2.2 *Kinetic analysis of photocatalytic degradation.* To elucidate the reaction mechanism and evaluate the photocatalytic performance of the synthesized samples, the degradation kinetics were analyzed using the pseudo-first-order (PFO) kinetic model (Fig. 10). The corresponding rate constants

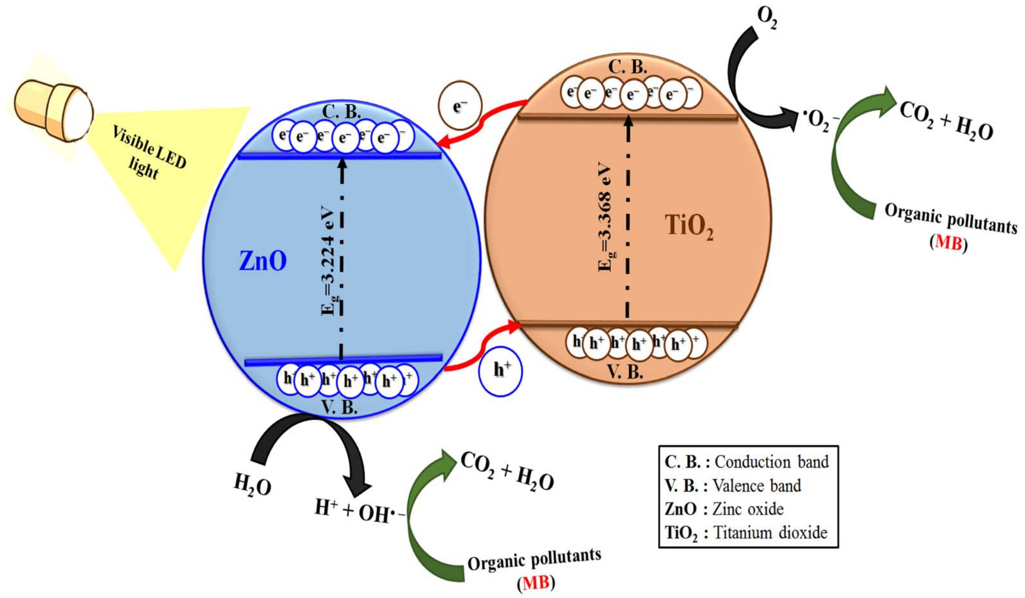

Fig. 11 A proposed photocatalytic mechanism for the $(1 - x)ZnO{:}(x)TiO_2$ catalyst.

(K_{app}), half-life times ($t_{1/2}$), and correlation coefficients (R^2) were determined and are presented in Table 5.

The photocatalytic degradation of MB in water using $(1-x)$ZnO:(x)TiO$_2$ under visible LED light (Fig. 10) was successfully fitted using the L–H model, and can be described by a pseudo-first order kinetic as confirmed by the obtained straight line.

The kinetic parameters obtained from the pseudo-first-order (PFO) model reveal meaningful trends in the photocatalytic degradation performance of the studied samples (Table 5). All samples exhibit high correlation coefficients (R^2 values ranging from 0.929 to 0.998), indicating a good fit of the experimental data to the PFO model and supporting its suitability for describing the MB degradation kinetics. Notably, the velocity constant k shows significant variation with doping concentration, reflecting changes in photocatalytic activity. For instance, ZnTi10% and ZnTi15% display markedly higher rate constants (0.0099 and 0.0119 min^{-1}, respectively) compared to ZnTi1% (0.0019 min^{-1}), suggesting enhanced degradation efficiency at higher doping levels. This enhancement can be attributed to improved charge separation, increased surface area, or modified electronic structures that facilitate pollutant interaction at the catalyst surface.[93] The corresponding half-life times ($t_{1/2}$) also reflect this trend, where higher k values are associated with shorter degradation times (*e.g.*, ZnTi15% shows a $t_{1/2}$ of 58 minutes), significantly lower than the 364 minutes observed for ZnTi1%. These results suggest an optimal doping range (10–15%) for maximizing photocatalytic efficiency, while very low doping levels may lead to insufficient activation or higher recombination rates.[94] Taken together, the consistency and physical relevance of the PFO parameters across all samples validate the choice of this model for further kinetic and mechanistic analysis in this study.

3.5.3. Principle of heterogeneous photocatalysis. When $(1-x)$ZnO:(x)TiO$_2$ samples were irradiated with light energy equal to or greater than its band-gap energy (E_g), electrons in the valence band (VB) are excited and transition to the conduction band (CB), creating electron–hole pairs.[27] These charge carriers then migrate to the surface of the photocatalyst, where the photofenerated electrons (e$^-$) typically reduce adsorbed oxygen molecules to superoxide radicals ($^{\bullet}O_2^-$), while the holes (h$^+$) oxidize water or hydroxyl groups to produce hydroxyle radicals ($^{\bullet}$OH).[29] Both these radicals are highly reactive species that play a crucial role in the degradation of organic pollutants.[29] This incorporation of TiO$_2$ into the ZnO lattice modifies the band structure and charge carrier dynamics, reducing recombination and thereby enhancing the overall photocatalytic activity.[29]

The following scenarios can occur during this process:

(1) Migration of photogenerated holes (h$^+$) to the catalyst surface, where they participate in oxidation reactions.

(2) Recombination of electron–hole pairs in the bulk of the material, which reduces photocatalytic efficiency.

(3) Migration of photogenerated electrons (e$^-$) to the catalyst surface, where they participate in reduction reactions.

(4) Recombination of charge carriers at the catalyst surface, which also reduces photocatalytic activity.[95]

The addition of TiO$_2$ into ZnO modifies the band-gap energy and charge carrier dynamics, as shown in Table 4. At low doping levels (*e.g.*, ZnTi1%), the band-gap energy decreases slightly (*e.g.*, 3.185 eV for direct transitions), which enhances light absorption in the visible region. This is attributed to the introduction of defect states (*e.g.*, oxygen vacancies) and lattice

Table 6 A comparison study of $(1-x)$ZnO:(x)TiO$_2$ powders with other recent similar photocatalysts material[a]

Samples	Dye	Dye con. (mg L^{-1})	Light irradiated	Time	Removal (%)	K_{app} (10^{-3} min^{-1})	Ref.
Cu-doped ZnO	MB	3.2	UV light	2 h	74	5.6	98
TiO$_2$-Ag NPs	RhB	5	Not mentioned	3.5 h	99.7	19.1	99
CuO/TiO$_2$	MB	5	Simulated sunlight	1 h	40	Not mentioned	100
TiO$_2$	MB	10	UV light	2 h	53.06	4.1	101
0.05Fe$_2$O$_3$/TiO$_2$	RhB	4.79	UV light	5 h	60	Not mentioned	102
Ag loaded TiO$_2$–ZnO	MB	10	UV light	2 h	70	9.92	103
ZnO@TiO$_2$	MB	10	Solar light irradiation	2 h	25	1.27	27
	MR				13	1.38	
(ZnO@TiO$_2$)	MB	10	18 W UV-lamp	2 h	59.56	6.64	104
ZnO@TiO$_2$ p–n junction	MO	32.73	Photoreactor	3 h	26.2	Not mentioned	105
					42.8		
ZnO	MB	10	Visible light irradiation	165 min	98.95	40.7	This work
ZnTi1%					38.63	1.9	
ZnTi2%					69.54	6.4	
ZnTi3%					42.72	2.7	
ZnTi5%					55.90	3.8	
ZnTi10%					83.63	9.9	
ZnTi15%					86.81	11.89	
TiO$_2$					93.18	13.34	

[a] Abbreviation: Methyl Orange (MO), Rhodamine B (RhB), Methylene Blue (MB), Methylene Red (MR), Oxidation (Ox), Reduction (Re).

distortions caused by Ti^{4+} ions.[87] For intermediate doping levels (*e.g.*, ZnTi10%), the formation of the Zn_2TiO_4 phase further modifies the electronic structure, leading to improved charge separation and reduced recombination rates.[96]

The photogenerated charge carriers (electrons and holes) drive redox reactions at the catalyst's surface:

- Electrons (e^-) in the conduction band reduce molecular oxygen (O_2) to form superoxide radicals ($^{\bullet}O_2^-$).
- Holes (h^+) in the valence band oxidize water (H_2O) or hydroxide ions (OH^-) to produce hydroxyl radicals ($OH^{\bullet}$).

These reactive species (*e.g.*, $^{\bullet}O_2^-$ and $OH^{\bullet}$) are highly oxidative and play a key role in the degradation of organic pollutants. The overall process can be summarized by the following reactions (Fig. 11):

(1) Excitation of TiO_2-doped ZnO by light:

$$\mathrm{ZnO{:}TiO_2} + h\nu \rightarrow \mathrm{e^-\ (CB)} + \mathrm{h^+\ (VB)}$$

(2) Reduction of oxygen by electrons:

$$\mathrm{e^-} + \mathrm{O_2} \rightarrow \mathrm{O_2}^{\bullet -}$$

(3) Oxidation of water/hydroxide by holes:

$$\mathrm{h^+} + \mathrm{OH^-} \rightarrow \mathrm{OH^{\bullet}}$$

(4) Degradation of pollutants:

$$\mathrm{OH^{\bullet}}\ \text{or}\ \mathrm{O_2}^{\bullet -} + \text{organic pollutants} \rightarrow \text{degradation products}$$

The hydroxyl radicals ($OH^{\bullet}$) and superoxide radicals ($O_2^{\bullet -}$) attack organic pollutants, breaking them down into simpler, less toxic compounds such as H_2O, CO_2 and N_2. This process contributes to environmental purification by removing harmful substances from water or air.[97]

Table 6 shows a summary of the doped/heterojunction/nanocomposite photocatalysts based ZnO@TiO_2, dye concentration, pollutant type, exposed light source, and photocatalytic performance.

4. Conclusion

In this study, $(1 - x)\mathrm{ZnO}{:}(x)\mathrm{TiO_2}$ composites were successfully synthesized using the solid-state sintering method. Structural analyses by X-ray diffraction confirmed the presence of the hexagonal wurtzite phase of ZnO at low TiO_2 contents, while increasing TiO_2 content led to the appearance of the anatase TiO_2 and spinel Zn_2TiO_4 phases. This structural evolution, accompanied by a decrease in crystallite size and deformation of the crystal lattice, confirms the effective integration of Ti^{4+} ions into the ZnO matrix. FTIR analyses reinforced these results by indicating the presence of characteristic Zn–O, Ti–O, and Zn–O–Ti bonds, highlighting interactions between the oxides. Electron microscopy reveals that Ti doping modifies the morphology of the particles, influencing their size and distribution. Optically, the incorporation of Ti slightly reduced the band gap, linked to lattice distortions and the appearance of crystal defects, although this reduction did not systematically improve the photocatalytic performances. Indeed, the photocatalytic study demonstrated that while pure ZnO and TiO_2 offer excellent methylene blue degradation efficiency under visible light irradiation, the doped samples exhibit lower performances, although the compositions containing $x \geq 0.1$ were distinguished by a notable activity, without however surpassing that of pure ZnO. These results suggest that the synergistic effect between ZnO, TiO_2, and Zn_2TiO_4 can promote charge separation and reduce electron–hole pair recombination, but that excessive doping or poor surface defect management can limit photocatalytic activity. Thus, this study demonstrates the complexity of the effect of Ti doping on ZnO properties and emphasizes the need for fine-tuning of synthesis conditions to improve its photocatalytic efficiency under visible light. Further work will be essential to better understand the relationship between structure, optical properties, and photocatalytic activity, particularly by exploring the influence of morphology, specific surface area, and operating conditions.

Conflicts of interest

The author declare that they have no conflict of interest. The author declare that they have no known competing financial interests or personal relationships that could have appeared to influence the work reported in this paper.

Data availability

The raw data (including excel files and experimental measurements) supporting the findings of this study are not publicly available due to confidentiality restrictions, but they can be provided by the corresponding author upon reasonable request.

Acknowledgements

The authors gratefully acknowledge the International Science Program (ISP) at Uppsala University, Sweden, for support through the African Network of Electroanalytical Chemists (IPICS/ANEC). We also thank The World Academy of Sciences (TWAS) for financial support under grant no. 16-499RG/CHE/AF/AC G-FR3240293299. Additionally, the authors from the Laboratory of Materials for Energy, Environment and Modeling (LM2EM, University of Sfax, Tunisia) acknowledge the support of the Tunisian Ministry of Higher Education and Scientific Research.

References

1 P. Panchal, *et al.*, Biogenic mediated Ag/ZnO nanocomposites for photocatalytic and antibacterial activities towards disinfection of water, *J. Colloid Interface Sci.*, 2020, **563**, 370–380.

2 D. Bhatia, *et al.*, Biological methods for textile dye removal from wastewater: A review, *Crit. Rev. Environ. Sci. Technol.*, 2017, **47**(19), 1836–1876.

3 A. M. Teli, *et al.*, Investigating the synergistic effects of NbCo-oxide composite electrodes in supercapacitor and water splitting applications via hydrothermal synthesis, *J. Energy Storage*, 2024, **86**, 111155.

4 Y. Zhang, *et al.*, Sensors for the environmental pollutant detection: Are we already there?, *Coord. Chem. Rev.*, 2021, **431**, 213681.

5 S. Zodi, *et al.*, Direct red 81 dye removal by a continuous flow electrocoagulation/flotation reactor, *Sep. Purif. Technol.*, 2013, **108**, 215–222.

6 P. Panchal, *et al.*, Biogenic mediated Ag/ZnO nanocomposites for photocatalytic and antibacterial activities towards disinfection of water, *J. Colloid Interface Sci.*, 2020, **563**, 370–380.

7 K. D. Bhalerao, *et al.*, Synthesis, characterizations, and hydrogen sulfide gas sensing application of BiOx (x= 1, 1.5) nanostructures, *Int. J. Hydrogen Energy*, 2023, **48**(2), 840–848.

8 N. Mintcheva, *et al.*, Gas sensing of laser-produced hybrid TiO2-ZnO nanomaterials under room-temperature conditions, *Nanomaterials*, 2023, **13**(4), 670.

9 M. Thomas and T. S. Natarajan, TiO2-high surface area materials based composite photocatalytic nanomaterials for degradation of pollutants: A review, *Photocatalytic nanomaterials for environmental applications*, 2018, 27, pp. 48–96.

10 C. B. Ong, L. Y. Ng and A. W. Mohammad, A review of ZnO nanoparticles as solar photocatalysts: Synthesis, mechanisms and applications, *Renew. Sustain. Energy Rev.*, 2018, **81**, 536–551.

11 A. Xiaoyan, *et al.*, Application of a new nano-TiO2 composite antibacterial agent in nursing management of operating room: Based on real-time information push assistant system, *Prev. Med.*, 2023, **172**, 107541.

12 S. Jiang, K. Lin and M. Cai, ZnO nanomaterials: current advancements in antibacterial mechanisms and applications, *Front. Chem.*, 2020, **8**, 580.

13 A. M. Teli, *et al.*, Innovations in metal telluride composite materials towards enhancing supercapacitor energy storage, *J. Alloys Compd.*, 2024, **1005**, 175950.

14 G. K. Upadhyay, *et al.*, Synthesis of ZnO: TiO2 nanocomposites for photocatalyst application in visible light, *Vacuum*, 2019, **160**, 154–163.

15 E. Y. Shaba, *et al.*, A critical review of synthesis parameters affecting the properties of zinc oxide nanoparticle and its application in wastewater treatment, *Appl. Water Sci.*, 2021, **11**(2), 48.

16 A. Rayerfrancis, *et al.*, Effect of pH on the morphology of ZnO nanostructures and its influence on structural and optical properties, *Phys. B*, 2015, **457**, 96–102.

17 V. Kumar, *et al.*, Multifunctional Aspects of Mechanical and Electromechanical Properties of Composites Based on Silicone Rubber for Piezoelectric Energy Harvesting Systems, *Polymers*, 2024, **16**(14), 2058.

18 P. Obreja, *et al.*, Influence of surface substrates on the properties of ZnO nanowires synthesized by hydrothermal method, *Appl. Surf. Sci.*, 2019, **463**, 1117–1123.

19 P. Amornpitoksuk, *et al.*, Synthesis, photocatalytic and antibacterial activities of ZnO particles modified by diblock copolymer, *Powder Technol.*, 2011, **212**(3), 432–438.

20 S. O. Ogunyemi, *et al.*, Green synthesis of zinc oxide nanoparticles using different plant extracts and their antibacterial activity against Xanthomonas oryzae pv. oryzae, *Artif. Cell Nanomed. Biotechnol.*, 2019, **47**(1), 341–352.

21 M. M. Tavakoli, *et al.*, Light management in organic photovoltaics processed in ambient conditions using ZnO nanowire and antireflection layer with nanocone array, *Small*, 2019, **15**(25), 1900508.

22 D. Chen, *et al.*, Self-powered ultraviolet photovoltaic photodetector based on graphene/ZnO heterostructure, *Appl. Surf. Sci.*, 2020, **529**, 147087.

23 D. Sinha, *et al.*, ZnO and TiO2 nanostructured dye sensitized solar photovoltaic cell, *Mater. Today: Proc.*, 2019, **11**, 782–788.

24 R. Ramadan, *et al.*, Sol–gel-deposited Ti-doped ZnO: Toward cell fouling transparent conductive oxides, *ACS Omega*, 2019, **4**(7), 11354–11363.

25 W. L. de Almeida, *et al.*, Study of structural and optical properties of ZnO nanoparticles synthesized by an eco-friendly tapioca-assisted route, *Mater. Chem. Phys.*, 2021, **258**, 123926.

26 V. Parihar, M. Raja and R. Paulose, A brief review of structural, electrical and electrochemical properties of zinc oxide nanoparticles, *Rev. Adv. Mater. Sci.*, 2018, **53**(2), 119–130.

27 H. M. Mousa, *et al.*, Synthesis of TiO2@ ZnO heterojunction for dye photodegradation and wastewater treatment, *J. Alloys Compd.*, 2021, **886**, 161169.

28 C. H. Nguyen, *et al.*, Enhanced removal of various dyes from aqueous solutions by UV and simulated solar photocatalysis over TiO2/ZnO/rGO composites, *Sep. Purif. Technol.*, 2020, **232**, 115962.

29 K. Xu, *et al.*, Construction of Ag-modified TiO 2/ZnO heterojunction nanotree arrays with superior photocatalytic and photoelectrochemical properties, *RSC Adv.*, 2020, **10**(57), 34702–34711.

30 V. Kumar, *et al.*, Lightweight, compressible, stretchable, ultra-soft, and mechanically stable composites for piezo-electric energy generators and strain sensing, *Mater. Res. Bull.*, 2024, **179**, 112962.

31 R. Yousefi, *et al.*, Synthesis and characterization of Pb-doped ZnO nanoparticles and their photocatalytic applications, *Mater. Res. Innovations*, 2016, **20**(2), 121–127.

32 I. Darmadi, A. Taufik and R. Saleh, Analysis of optical and structural properties of Ti-doped ZnO nanoparticles synthesized by co-precipitation method, *J. Phys.: Conf. Ser.*, 2020, **1442**, 012021.

33 S. Ayed, *et al.*, Solid state synthesis and structural characterization of zinc titanates, *J. Alloys Compd.*, 2016, **677**, 185–189.

34 I. Khan, *et al.*, Review on methylene blue: Its properties, uses, toxicity and photodegradation, *Water*, 2022, **14**(2), 242.

35 M. A. Habib, *et al.*, Synthesis and characterization of ZnO-TiO2 nanocomposites and their application as photocatalysts, *Int. Nano Lett.*, 2013, **3**(1), 5.

36 A. H. Ajil, *et al.*, Enhancing methyl orange degradation with laser-generated ZnO and Ce-doped ZnO nanoparticles, *Appl. Sci.*, 2023, **13**(21), 11857.

37 K. Khan, *et al.*, Effect of TiO2 on surface spins disorder of MgFe2O4 nanoparticles, *Appl. Phys. A*, 2023, **129**(1), 2.

38 F. Z. Janani, *et al.*, ZnO-Zn2TiO4 heterostructure for highly efficient photocatalytic degradation of pharmaceuticals, *Environ. Sci. Pollut. Res.*, 2023, **30**(34), 81403–81416.

39 D. Štrbac, *et al.*, Photocatalytic degradation of Naproxen and methylene blue: Comparison between ZnO, TiO2 and their mixture, *Process Saf. Environ. Prot.*, 2018, **113**, 174–183.

40 P. Chaiyo, *et al.*, Electrical and sensitivity properties of ZnO/TiO2 heterojunction nanocomposites for ammonia gas sensor, *J. Phys.: Conf. Ser.*, 2019, **1259**, 012005.

41 T. A. Altalhi, Original strategy for facile synthesis of hybrid 'ZnO–Zn2TiO4'nanotubes and antimicrobial activity, *Mater. Res. Express*, 2018, **5**(10), 105001.

42 B. Zhu, *et al.*, Improvement in gas sensitivity of ZnO thick film to volatile organic compounds (VOCs) by adding TiO2, *Mater. Lett.*, 2004, **58**(5), 624–629.

43 O. Muktaridha, *et al.*, Progress of 3d metal-doped zinc oxide nanoparticles and the photocatalytic properties, *Arab. J. Chem.*, 2021, **14**(6), 103175.

44 P. Raji and K. B. Kumar, Investigation of Ti doping on the structural, optical, and magnetic properties of ZnO nanoparticles, *J. Mater. Sci.: Mater. Electron.*, 2021, **32**(9), 11751–11762.

45 A. Toghan, K. K. Taha and A. Modwi, TiO2–ZnO composites fabricated via sonication assisted with gelatin for potential use in Rhodamine B degradation, *J. Mater. Sci.: Mater. Electron.*, 2021, **32**(2), 2471–2485.

46 M. Ashok kumar and S. Muthukumaran, Effect of solvents on the structural, optical and morphological properties of ZnCuO nanoparticles, *J. Mater. Sci.: Mater. Electron.*, 2013, **24**(10), 4050–4059.

47 M. S. Hossain and S. Ahmed, Easy and green synthesis of TiO2 (Anatase and Rutile): Estimation of crystallite size using Scherrer equation, Williamson-Hall plot, Monshi-Scherrer Model, size-strain plot, Halder-Wagner Model, *Results Mater.*, 2023, **20**, 100492.

48 M. Xin, Crystal structure and optical properties of ZnO: Ce nano film, *Molecules*, 2022, **27**(16), 5308.

49 P. Norouzzadeh, *et al.*, Comparative study on dielectric and structural properties of undoped, Mn-doped, and Ni-doped ZnO nanoparticles by impedance spectroscopy analysis, *J. Mater. Sci.: Mater. Electron.*, 2020, **31**(10), 7335–7347.

50 V. G. Krishnan, *et al.*, Noticeable improvement in the toxic gas-sensing activity of the Zn-doped TiO 2 films for sensing devices, *New J. Chem.*, 2021, **45**(23), 10488–10495.

51 S. Lin, L. Songyuan and F. Yaochong, Facile preparation of ZnO/TiO 2 nanocomposite photocatalysts and study of their photocatalytic performance, *J. Ovonic Res.*, 2023, **19**, 739–761.

52 N. Kiomarsipour and R. S. Razavi, Hydrothermal synthesis of ZnO nanopigments with high UV absorption and vis/NIR reflectance, *Ceram. Int.*, 2014, **40**(7), 11261–11268.

53 S. Alamdari, *et al.*, Preparation and characterization of zinc oxide nanoparticles using leaf extract of Sambucus ebulus, *Appl. Sci.*, 2020, **10**(10), 3620.

54 J. Arin, *et al.*, Characterization of ZnO–TiO2 and zinc titanate nanoparticles synthesized by hydrothermal process, *Res. Chem. Intermed.*, 2017, **43**(5), 3183–3195.

55 Y. S. Kurniawan and L. Yuliati, Activity enhancement of p25 titanium dioxide by zinc oxide for photocatalytic phenol degradation, *Bull. Chem. React. Eng. Catal.*, 2021, **16**(2), 310–319.

56 L. Munguti and F. Dejene, Effects of Zn: Ti molar ratios on the morphological, optical and photocatalytic properties of ZnO-TiO2 nanocomposites for application in dye removal, *Mater. Sci. Semicond. Process.*, 2021, **128**, 105786.

57 S. J. Raphael, *et al.*, Investigation of Zn2TiO4 as fluorescence quenching probe for sensing of metal ions, *Results Surf. Interfaces*, 2023, **12**, 100127.

58 T. Ivanova, *et al.*, Preparation and characterization of ZnO–TiO2 films obtained by sol-gel method, *J. Non-Cryst. Solids*, 2011, **357**(15), 2840–2845.

59 A. Röckert, J. Kullgren and K. Hermansson, Predicting Frequency from the External Chemical Environment: OH Vibrations on Hydrated and Hydroxylated Surfaces, *J. Chem. Theory Comput.*, 2022, **18**(12), 7683–7694.

60 U. Qumar, *et al.*, Photocatalysis vs adsorption by metal oxide nanoparticles, *J. Mater. Sci. Technol.*, 2022, **131**, 122–166.

61 G. Rangarajan, A. Jayaseelan and R. Farnood, Photocatalytic reactive oxygen species generation and their mechanisms of action in pollutant removal with biochar supported photocatalysts: A review, *J. Clean. Prod.*, 2022, **346**, 131155.

62 L. Borkovska, *et al.*, The effect of TiO2 crystalline phase on microstructure and optical features of Zn2TiO4 doped with Mn, *J. Cryst. Growth*, 2024, **630**, 127603.

63 R. Ade, *et al.*, Enhanced optoelectronic properties of Ti-doped ZnO nanorods for photodetector applications, *Ceram. Int.*, 2021, **47**(17), 24031–24038.

64 S. A. Bidier, M. Hashim and M. Bououdina, Structural and optical characteristics of Ti-doped ZnO nanorods deposited by simple chemical bath deposition, *J. Mater. Sci.: Mater. Electron.*, 2017, **28**(15), 11178–11185.

65 M. A. B. Aissa, *et al.*, Facile synthesis of TiO2@ ZnO nanoparticles for enhanced removal of methyl orange and indigo carmine dyes: Adsorption, kinetics, *Heliyon*, 2024, (10), e31351.

66 Y. Pan, *et al.*, Influences of average particle size and non-uniformity on the statistical roughness characteristics of gravel-bed surfaces, *Arabian J. Geosci.*, 2022, **15**(11), 1021.

67 Y. Ding, *et al.*, Nanoporous TiO2 spheres with tailored textural properties: controllable synthesis, formation mechanism, and photochemical applications, *Prog. Mater. Sci.*, 2020, **109**, 100620.

68 K. N. Abbas and N. Bidin, Morphological driven photocatalytic activity of ZnO nanostructures, *Appl. Surf. Sci.*, 2017, **394**, 498–508.
69 A. Irshad, *et al.*, Unveiling the power of TiO2 doped ZnO nanomaterial as an effective antimicrobial solution in the leather industry, *Heliyon*, 2024, **10**, e38414.
70 L. Munguti and F. Dejene, Influence of annealing temperature on structural, optical and photocatalytic properties of ZnO–TiO2 composites for application in dye removal in water, *Nano-Struct. Nano-Objects*, 2020, **24**, 100594.
71 M. B. M. de Campos, *et al.*, Influence of terbium (III) ions on the photocatalytic activity of TiO2 and CeO2 for the degradation of methylene blue in industrial effluents, *Environ. Sci. Pollut. Res.*, 2021, **28**(21), 27147–27161.
72 K. Kaviyarasu, *et al.*, In vitro cytotoxicity effect and antibacterial performance of human lung epithelial cells A549 activity of zinc oxide doped TiO2 nanocrystals: investigation of bio-medical application by chemical method, *Mater. Sci. Eng., C*, 2017, **74**, 325–333.
73 M. Alias, K. M. Rashid and K. Adem, Optical properties for Ti doped thin Zno films prepared by PLD, *Int. J. Innov. Res. Sci. Eng. Technol.*, 2014, 3(8), 15538–15544.
74 B. Mehmood, *et al.*, Structural and optical properties of Ti and Cu co-doped ZnO thin films for photovoltaic applications of dye sensitized solar cells, *Int. J. Energy Res.*, 2021, **45**(2), 2445–2459.
75 S. Ayed, *et al.*, Structural and optical properties of ZnO/TiO2 composites, *Superlattices Microstruct.*, 2016, **91**, 118–128.
76 M. Naeem, *et al.*, Study of active surface defects in Ti doped ZnO nanoparticles, *J. Appl. Phys.*, 2010, **107**, 123520.
77 N. M. Rasdi, *et al.*, Effects of cobalt doping on structural, morphological, and optical properties of Zn2SiO4 nanophosphors prepared by sol-gel method, *Results Phys.*, 2017, **7**, 3820–3825.
78 A. Falamas, *et al.*, Size-dependent spectroscopic insight into the steady-state and time-resolved optical properties of ZnO photocatalysts, *Mater. Sci. Semicond. Process.*, 2022, **145**, 106644.
79 Y. Nosaka and A. Y. Nosaka, Reconsideration of Intrinsic Band Alignments within Anatase and Rutile TiO_2, *J. Phys. Chem. Lett.*, 2016, **7**, 431–434.
80 K. M. Reddy, S. V. Manorama and A. R. Reddy, Bandgap studies on anatase titanium dioxide nanoparticles, *Mater. Chem. Phys.*, 2003, **78**(1), 239–245.
81 J. Samuel, *et al.*, Characterization and antibacterial activity of Ti doped ZnO nanorods prepared by hydrazine assisted wet chemical route, *Phys. E*, 2022, **143**, 115374.
82 L.-D. Yuan, *et al.*, Unified theory of direct or indirect band-gap nature of conventional semiconductors, *Phys. Rev. B*, 2018, **98**(24), 245203.
83 I. Soumahoro, *et al.*, Structural, optical, spectroscopic and electrical properties of Mo-doped ZnO thin films grown by radio frequency magnetron sputtering, *Thin Solid Films*, 2014, **566**, 61–69.
84 P. S. Sundaram, S. S. R. Inbanathan and G. Arivazhagan, Structural and optical properties of Mn doped ZnO nanoparticles prepared by co-precipitation method, *Phys. B*, 2019, **574**, 411668.
85 S. Selvinsimpson, *et al.*, Synergetic effect of Sn doped ZnO nanoparticles synthesized via ultrasonication technique and its photocatalytic and antibacterial activity, *Environ. Res.*, 2021, **197**, 111115.
86 J. Zhao, *et al.*, Structure and photocatalytic activity of Ni-doped ZnO nanorods, *Mater. Res. Bull.*, 2011, **46**(8), 1207–1210.
87 S. Lettieri, *et al.*, Charge carrier processes and optical properties in TiO2 and TiO2-based heterojunction photocatalysts: A review, *Materials*, 2021, **14**(7), 1645.
88 X. Zhan, *et al.*, Investigation of the reaction kinetics of photocatalytic pollutant degradation under defined conditions with inkjet-printed TiO 2 films–from batch to a novel continuous-flow microreactor, *React. Chem. Eng.*, 2020, **5**(9), 1658–1670.
89 H. Zeghioud, *et al.*, Photocatalytic reactors dedicated to the degradation of hazardous organic pollutants: kinetics, mechanistic aspects, and design–a review, *Chem. Eng. Commun.*, 2016, **203**(11), 1415–1431.
90 R. H. A. Murti, *et al.*, High efficiency on resin photocatalysis: Study on application and kinetic mechanism using langmuir Hinshelwood Model, *S. Afr. J. Chem. Eng.*, 2025, **53**, 87–95.
91 H. D. Tran, *et al.*, Kinetics of photocatalytic degradation of organic compounds: a mini-review and new approach, *RSC Adv.*, 2023, **13**(25), 16915–16925.
92 K. V. Kumar, K. Porkodi and Rocha, Langmuir–Hinshelwood kinetics–a theoretical study, *Catal. Commun.*, 2008, **9**(1), 82–84.
93 W. Zhao, *et al.*, A critical review on surface-modified nano-catalyst application for the photocatalytic degradation of volatile organic compounds, *Environ. Sci.: Nano*, 2022, **9**(1), 61–80.
94 Y. Zhang, *et al.*, Internal quantum efficiency higher than 100% achieved by combining doping and quantum effects for photocatalytic overall water splitting, *Nat. Energy*, 2023, **8**(5), 504–514.
95 Q. Guo, *et al.*, Fundamentals of TiO2 photocatalysis: concepts, mechanisms, and challenges, *Adv. Mater.*, 2019, **31**(50), 1901997.
96 A. Gaurav, *et al.*, Study on the effect of copper ion doping in zinc oxide nanomaterials for photocatalytic applications, *Mater. Chem. Phys.*, 2019, **230**, 162–171.
97 R. A. Gonçalves, *et al.*, Green synthesis and applications of ZnO and TiO2 nanostructures, *Molecules*, 2021, **26**(8), 2236.
98 F. Mo, Q. Zhou and Y. He, Nano–Ag: Environmental applications and perspectives, *Sci. Total Environ.*, 2022, **829**, 154644.
99 J. Cuadra, *et al.*, Multifunctional silver-coated transparent TiO2 thin films for photocatalytic and antimicrobial applications, *Appl. Surf. Sci.*, 2023, **617**, 156519.
100 Z. Ren, *et al.*, Facile synthesis of ZnO/ZnS heterojunction nanoarrays for enhanced piezo-photocatalytic performance, *Mater. Lett.*, 2021, **292**, 129635.

101 F. Nouasria, *et al.*, Improvement of the photocatalytic performance of ZnO thin films in the UV and sunlight range by Cu doping and additional coupling with Cu2O, *Ceram. Int.*, 2022, **48**(9), 13283–13294.

102 A. Kumar, *et al.*, A dual effect of surface roughness and photocatalysis of crystalline TiO2-thin film for self-cleaning application on a photovoltaic covering glass, *Mater. Chem. Phys.*, 2022, **289**, 126427.

103 S. Wannapop, A. Somdee and T. Bovornratanaraks, Experimental study of thin film Fe2O3/TiO2 for photocatalytic Rhodamine B degradation, *Inorg. Chem. Commun.*, 2021, **128**, 108585.

104 A. Haghighatzadeh, *et al.*, Improved photocatalytic activity of ZnO-TiO2 nanocomposite catalysts by modulating TiO2 thickness, *Mater. Res. Express*, 2019, **6**(11), 115060.

105 S. Chen, *et al.*, Preparation, characterization and activity evaluation of p–n junction photocatalyst p-ZnO/n-TiO2, *Appl. Surf. Sci.*, 2008, **255**(5), 2478–2484.